



Global stability and bifurcation of macroscopic traffic flow models for upslope and downslope

Bing-Ling Cen · Yu Xue  · Yan-Feng Qiao · Yi Wang · Wei Pan · Hong-Di He

Received: 22 April 2022 / Accepted: 17 October 2022 / Published online: 20 November 2022
© The Author(s), under exclusive licence to Springer Nature B.V. 2022

Abstract A macro-continuum model of the traffic flow is derived from a micro-car-following model that considers both the upslope and downslope by using the transformation relationship between macro- and micro-variables. The perturbation propagation characteristics and stability conditions of the macroscopic continuum equation are discussed. For uniform flow in the initial equilibrium state, the stability conditions reveal that as the slope angle increased under the action of a small disturbance, the upslope stability increases and downslope stability decreases. Moreover, under a large disturbance, the global stability analysis is carried out by using the wavefront expansion technique for uniform flow in the initial equilibrium state. For the initial nonuniform flow, nonlinear bifurcation analysis such as Hopf bifurcation and saddle–node bifurcation is carried out at the

equilibrium point. Subcritical Hopf bifurcation exists when the traffic flow state changes; thus, the limit cycle formed by the Hopf bifurcation is unstable. And the existence condition of saddle-node bifurcation is obtained. Simulation results verify the stability conditions of the model and determine the critical density range. The numerical simulation results show the existence of Hopf bifurcation in phase space, and the spiral saddle point of saddle-node bifurcation varies with the slope angle. Furthermore, the impact of the angle of both the upslope and downslope on the evolution of density waves is investigated.

Keywords Upslope and downslope · Stability condition · Wavefront expansion · Hopf bifurcation

B.-L. Cen · Y. Xue (✉) · Y.-F. Qiao · Y. Wang
Institute of Physical Science and Technology, Guangxi
University, Nanning 53004, China
e-mail: yuxuegxu@gxu.edu.cn

W. Pan
Guangxi Medical University, Nanning 530021,
Guangxi, China

H.-D. He
Center for Intelligent Transportation Systems and
Unmanned Aerial Systems Applications, State Key
Laboratory of Ocean Engineering, School of Naval
Architecture, Ocean and Civil Engineering, Shanghai Jiao
Tong University, Shanghai 200240, China

1 Introduction

With the rapid development of city traffic systems and increasing number of vehicles, examination of the mechanism of traffic congestion and establishment of methods to contain this phenomenon are becoming increasingly challenging [1–5]. In the recent decade, a variety of traffic models, such as the car-following model [6–8], cellular automaton model [4], gas-kinetic model [5] and hydrodynamic model or continuum model [9–24], have been developed. Many researchers have applied traffic flow models to study the influence of road conditions on driving behavior,

such as honking [25], visibility in fog [26] and curves [27], etc.

Empirical observations over many years indicate that various congested traffic patterns are induced by traffic bottlenecks on roads [28, 29]. Helbing and Lee et al. [15, 29, 30] observed many congested traffic patterns caused by traffic bottlenecks, such as pinned localized clusters (PLCs), triggered stop-and-go waves (TSGs), oscillating congested traffic (OCT), homogeneous synchronized traffic (HST), and homogeneous congested traffic (HCT), via numerical simulations. Notably, uphill and downhill roads represent a type of traffic bottleneck, and the traffic congestion caused by these entities has attracted the attention of traffic engineers and researchers. In 2009, Komada studied vehicles in the context of the gravitational force on sloped roads to extend the optimal velocity model by considering upslope and downslope gradients and clarified the traffic states and jamming transitions induced by the slopes of sags and hills [31]. Zhu et al. focused on the impact of the slope angle on traffic stability and investigated the stability condition and density waves of the traffic flow on a single lane gradient (upslope or downslope) [32]. Wu et al. examined the steady-state traffic flow on a ring road with upslopes and downslopes by using a semidiscrete model [33]. Gupta et al. studied a unidirectional single lane gradient highway by using the optimal flow differential method for a lattice hydrodynamic model [34]. Kaur and Sharma proposed a lattice hydrodynamics model of traffic flow and conducted a simulation study by considering the anticipation effect of drivers in a two-lane traffic system on a slope curve [35]. Moreover, many extension models have been proposed. For example, Li et al. considered the driver habit, slope grade and slope length [36]. Yu et al. focused on the effect of the variable slope [37]. Chen investigated the slope of two-lanes [38], Tan et al. considered the effect of low-visibility foggy weather on a highway with slopes [39], and other researchers considered several relevant factors [40–44]. With the development of transportation theory and technology, the research of intelligent transportation system has been carried out in recent years [45–47]. Nevertheless, the traffic congestion caused by uphill and downhill slopes has not been simultaneously considered. Due to the different uphill and downhill movement states, the traffic flow may be unstable, and complex traffic congestion may occur.

To examine the traffic congestion caused by uphill and downhill slopes, we attempt to establish a macroscopic fluid dynamics model of uphill and downhill slopes by transforming the microscopic model to a macroscopic model. In 2000, Berg et al. established a continuum approach for car-following models by deriving the relation of the headway of successive vehicles with the density [48]. The car-following model and continuum model can be integrated. Helbing derived nonlocal macroscopic traffic equations from microscopic car-following models by using gradient expansion, linear interpolation and the smooth particle hydrodynamics approach [49]. Gupta et al. expressed the headway as a perturbation series, obtained an anisotropic higher-order continuum model, and studied the formation of shock and rarefaction waves, the local cluster, and the generation of stop-and-go traffic [50, 51].

In this study, we focus on not only the stability of the small disturbance range near the equilibrium state but also attempt to analyze the global stability and state bifurcation of traffic flow. Yi et al. [52], Ou et al. [53] and Gupta et al. [54] studied the nonlinear stability criterion of macroscopic traffic flow models by using a wavefront expansion technique under large traffic disturbances. To examine the traffic flow bifurcation, Carrillo et al. [55] demonstrated the occurrence of Bogdanov–Takens bifurcations in a two-parameter dynamic system for Kerner–Konhäuser’s model. In 2015, Delgado et al. [56] proved the existence of degenerate Bogdanov–Takens bifurcations for Kerner–Konhäuser’s model, thereby explaining the presence of Hopf bifurcation. In 2004, Gasser et al. [57] analyzed the bifurcation characteristics of car-following models. They demonstrated that Hopf bifurcation generally leads to instability of quasistationary solutions in the optimal velocity model, and obtained a criterion pertaining to the sub- or supercriticality of the Hopf bifurcation. In 2004 and 2006, Orosz et al. [58–60] investigated Hopf bifurcation for a single fixed time-delay differential equations like a car-following model considering reaction time delay. Similarly, their results show that Hopf bifurcation reduces the stability of the system and subcritical Hopf bifurcations may cause bistability. In 2020, Ngoduy et al. [61] established a general bifurcation structure of a car-following model with multiple time delays. The impact of multiple time delays and other model parameters on the Hopf bifurcation in various existing car-following models with delays was

discussed. In 2015, Ai et al. [62] considered that bifurcation corresponds to traffic jams by the bifurcation analysis for a speed gradient macro-continuum traffic flow model. More recently, Miura et al. [63] observed macroscopic collective phenomenon that occur only in multi-body systems while studying bifurcations in optimal velocity models. The authors noted the traffic jams occur as a moving cluster in the bifurcation structure. Ren et al. [64] studied the conditions for occurrence and stability of Hopf bifurcation for heterogeneous continuum traffic flow and explained that stop-and-go traffic corresponds to Hopf bifurcation. The study of traffic flow stability helps to reveal the condition of traffic change, and the bifurcation of traffic state indicates the instability of the equilibrium state of the traffic system. Nevertheless, the research on the bifurcation behaviors of traffic state caused by road conditions such as upslope and downslope, road curves etc. is still limited from the perspective of macroscopic traffic flow model. The traffic stability caused by these different traffic conditions such as uphill, downhill, road reduction and curve type of traffic bottleneck is different. Traffic stability in these road conditions is related to traffic vehicle factors and road conditions. Therefore, it is worth exploring the relationship between traffic instability and traffic bifurcation. Different from the microscopic model, the macroscopic continuum model is applied to study the bifurcation, chaos and other nonlinear behaviors of traffic congestion formation and dissipation caused by road constraints.

In this paper, we derive the macroscopic continuum model of uphill and downhill slopes by transforming the microscopic model to a macroscopic model, as described in Sect. 2, and deduce the stability condition through a linear analysis. As described in Sect. 3, a global stability analysis is conducted using the wave-front expansion method. Section 4 discusses the conditions for the presence of Hopf bifurcation and saddle-node bifurcation. Section 5 describes the numerical simulation performed to explore the evolution of traffic density waves. Finally, the concluding remarks are presented.

2 Proposed model

Figure 1 shows the schematic of a vehicle on a slope subjected to gravitational force. The angles of the



Fig. 1 Schematic of the gravitational force upon a vehicle on the slope gradient

slope are represented by θ , the gravitation acceleration is g , and the vehicle has a mass m . According to Newton’s second law,

$$m \frac{d^2 x_i(t)}{dt^2} = F(\Delta x_i) - \mu \frac{dx_i(t)}{dt} - mg \sin \theta S(x_i) \quad (1)$$

where $\Delta x_i (= x_{i+1} - x_i)$ is the headway, $F(\Delta x_i)$ is the driving force contributed by the vehicle engine, μ denotes the friction coefficient, and $S(x_i)$ represents the slope-control function, with $S(x_i) = 1$ and $S(x_i) = -1$ for the upslope and downslope, respectively.

An extended optimal velocity model including the effect of the slope in comparison with the optimal velocity model can be defined as follows [8]:

$$\frac{d^2 x_i(t)}{dt^2} = a \left\{ V_0(\Delta x_i, x_i) - \frac{dx_i(t)}{dt} \right\} \quad (2)$$

where $a (= \mu/m)$ is the sensitivity, the inverse of which corresponds to the delay time τ , with $V_0(\Delta x_i, x_i) = \frac{F(\Delta x_i)}{\mu} - \frac{mg \sin \theta S(x_i)}{\mu}$. The optimal velocity function is specified with reference to the work of Gupta et al. [34]:

$$V_0(\Delta x_i) = \left(\frac{v_{\max}}{2} - \frac{v_{\text{up},\max}}{2} \right) \left[\tanh(\Delta x_i - x_{c,\text{up}}(\theta)) + \tanh(x_{c,\text{up}}(\theta)) \right] \quad (3)$$

For an upslope gradient highway, $S(x_i) = 1$, with

$$V_0(\Delta x_i) = \left(\frac{v_{\max}}{2} + \frac{v_{\text{down},\max}}{2} \right) \left[\tanh(\Delta x_i - x_{c,\text{down}}(\theta)) + \tanh(x_{c,\text{down}}(\theta)) \right] \quad (4)$$

and for a downslope gradient highway, $S(x_i) = -1$, where $v_{\text{up},\max}$ and $v_{\text{down},\max}$ denote the maximal reduced and enhanced velocities on the upslope and downslope, respectively, and $v_{\text{up},\max} = v_{\text{down},\max} = mg \sin \theta / \mu$ [34]. As the slope angle increases, the safe distance on the upslope (downslope) decreases

(increases). In particular, $x_{c,up} = x_c(1 - \alpha \sin \theta)$, $x_{c,down} = x_c(1 + \beta \sin \theta)$, and for simplicity, $\alpha = \beta = 1$, which leads to $x_{c,up} = x_c(1 - \sin \theta)$, $x_{c,down} = x_c(1 + \sin \theta)$ [32]. The following approximate equation is defined:

$$V_0(\Delta x_i, x_i) = \left(1 - \frac{S(x_i)mg \sin \theta}{\mu v_{max}}\right) \frac{v_{max}}{2} [\tanh(\Delta x_i - x_{c,g}) + \tanh(x_{c,g})] \tag{5}$$

For simplicity, $mg/\mu v_{max} = 1$, and $V_0(\Delta x_i, x_i) = \gamma V(\Delta x_i, x_i)$. Here the slope Angle parameter $\gamma = 1 - S(x_i) \sin \theta$, $V(\Delta x_i, x_i) = \frac{v_{max}}{2} [\tanh(\Delta x_i - x_{c,g}) + \tanh(x_{c,g})]$, and $x_{c,g} = x_c(1 - S(x_i) \sin \theta)$.

Substituting the above expressions, Eq. (2) can be simplified as

$$\frac{d^2 x_i(t)}{dt^2} = a \left\{ \gamma V(\Delta x_i) - \frac{dx_i(t)}{dt} \right\} \tag{6}$$

According to continuum approach to car-following models, transformation relating headway Δx_i to density ρ enables predictions of the global effect and characteristics of microscopic model. The microscopic transformation formulas are converted to macroscopic formulas, defined as [48]

$$x_i(t) \rightarrow x(x, t) \tag{7}$$

$$\frac{dv}{dt} \rightarrow \frac{\partial v}{\partial t} + v \frac{\partial v}{\partial x} \tag{8}$$

$$V(\Delta x_i) \rightarrow \bar{V}(\rho) + \bar{V}'(\rho) \left[\frac{\rho_x}{2\rho} + \frac{\rho_{xx}}{6\rho^2} \right] \tag{9}$$

where ρ denotes the local density. By the relation from the microscopic to macroscopic transformation, the function $S(x_i)$ becomes $S(x) = 1$ for upslope, $S(x) = -1$ for a downslope. In this manner, the governing equation of the macroscopic traffic model considering the upslope and downslope can be obtained:

$$\frac{\partial \rho}{\partial t} + \frac{\partial(\rho v)}{\partial x} = 0 \tag{10}$$

$$\frac{\partial v}{\partial t} + v \frac{\partial v}{\partial x} = a(\gamma \bar{V}(\rho) - v) + a\gamma \bar{V}'(\rho) \left(\frac{\rho_x}{2\rho} + \frac{\rho_{xx}}{6\rho^2} \right) \tag{11}$$

The full differentials of density and velocity: $d\rho = \rho_x dx + \rho_t dt$, $dv = v_x dx + v_t dt$ [54], and Eqs. (10) and (11) are rewritten in the matrix form:

$$\begin{bmatrix} 1 & v & 0 & \rho \\ 0 & -\frac{a\gamma \bar{V}'(\rho)}{2\rho} & 1 & v \\ dt & dx & 0 & 0 \\ 0 & 0 & dt & dx \end{bmatrix} \begin{bmatrix} \rho_t \\ \rho_x \\ v_t \\ v_x \end{bmatrix} = \begin{bmatrix} 0 \\ a(\gamma \bar{V}(\rho) - v) + a\gamma \bar{V}'(\rho) \frac{\rho_{xx}}{6\rho^2} \\ d\rho \\ dv \end{bmatrix} \tag{12}$$

The coefficient matrix of partial derivatives must be singular. Thus, the characteristic velocity can be derived as $(dx/dt)_{1,2} = v \pm \sqrt{-2a(1 \mp \sin \theta)\bar{V}'(\rho)}/2$, where $\bar{V}'(\rho) < 0$. Two characteristic velocities exist, which are smaller and larger than the local velocity v . This aspect indicates that high-order models exhibit an isotropic traffic flow because the characteristic velocities are greater than the local velocities [16]. However, for most second-order traffic models, Yi et al. [52] demonstrated that the disturbance wave propagating forward, which travels faster than traffic, promptly disappears. Moreover, most of the second-order models have been used in practice and known to effectively capture several important characteristics of traffic. Therefore, research on the dynamic behavior induced by uphill and downhill roads may have implications for practical applications.

The following stability conditions can be obtained by the linear analysis of Eqs. (10) and (11).

$$a > -2\gamma \rho_0^2 \bar{V}'(\rho_0) \tag{13}$$

For the upslope,

$$a > -2(1 - \sin \theta) \rho_0^2 \bar{V}'(\rho_0) \tag{14}$$

For the downslope,

$$a > -2(1 + \sin \theta) \rho_0^2 \bar{V}'(\rho_0) \tag{15}$$

where ρ_0 is the initial density. When the stability condition is violated, the stability of the uniform traffic flow in equilibrium is lost. According to stability condition (14), in the upslope case, the increase in the slope angle can enhance the stability of traffic flow. In

contrast, in the case of a downhill slope, the increase in the slope angle, as indicated in Eq. (15), deteriorates the stability of the traffic flow. This conclusion is consistent with the theoretical analysis of Zhu et al. [32] and Gupta et al. [34].

3 Global stability analysis

Yi et al. [52], Ou et al. [53] and Gupta et al. [54] studied the nonlinear stability criterion of a macroscopic traffic flow model by using a wavefront expansion technique under large traffic disturbances. In particular, Yi et al. [52] discussed the propagation stability conditions for second-order traffic flow. Ou et al. [53] and Gupta et al. [54] performed global stability analyses for an anisotropic macroscopic traffic flow model. As described in this section, we conduct a global stability analysis for the governing equations, Eqs. (10) and (11), under large traffic disturbances. By the following coordinate transformation, the solution of the traffic system is expanded around the wavefront in powers of ξ .

$$\xi = x - X(t) \tag{16}$$

where $X(t)$ indicates the location of the wavefront at time t . The characteristic velocity of the wavefront can be obtained at the equilibrium state:

$$\dot{X}(t) = \left(\frac{dx}{dt}\right)_{1,2} |_{(\rho_0, v_0)} = v \pm \frac{\sqrt{-2a\gamma\bar{V}'(\rho)}}{2} |_{(\rho_0, v_0)} \tag{17}$$

The local density ρ and local velocity v behind the wavefront can be expressed in the power series of ξ as follows:

$$\rho(x, t) = \rho_0 + \xi\rho_1(t) + \frac{1}{2}\xi^2\rho_2(t) + \dots \tag{18}$$

$$v(x, t) = v_0 + \xi v_1(t) + \frac{1}{2}\xi^2 v_2(t) + \dots \tag{19}$$

where $\rho_i(t) = \frac{\partial^i \rho}{\partial x^i} |_{(X(t)^-, t)}$, $v_i(t) = \frac{\partial^i v}{\partial x^i} |_{(X(t)^-, t)}$, $i = 1, 2, 3, \dots$. By applying Eqs. (18) and (19), the spatiotemporal partial derivative of the density ρ and velocity v can be calculated as follows:

$$\begin{aligned} \rho_t &= -\dot{X}(t)\rho_1(t) + \xi\dot{\rho}_1(t) - \xi\dot{X}(t)\rho_2(t) + \frac{1}{2}\xi^2\dot{\rho}_2(t) \\ &+ \dots \end{aligned} \tag{20}$$

$$\rho_x = \rho_1(t) + \xi\rho_2(t) + \frac{1}{2}\xi^2\rho_3(t) + \dots \tag{21}$$

$$v_t = -\dot{X}(t)v_1(t) + \xi\dot{v}_1(t) - \xi\dot{X}(t)v_2(t) + \frac{1}{2}\xi^2\dot{v}_2(t) + \dots \tag{22}$$

$$v_x = v_1(t) + \xi v_2(t) + \frac{1}{2}\xi^2 v_3(t) + \dots \tag{23}$$

Accordingly, the equilibrium velocity $\bar{V}(\rho, v)$ can be obtained.

$$\bar{V}(\rho, v) = \bar{V}^0 + \xi\left(\bar{V}_\rho^0\rho_1(t) + \bar{V}_v^0v_1(t)\right) + \dots \tag{24}$$

where $\bar{V}^0 = \bar{V}(\rho_0)$, $\bar{V}_\rho^0 = \frac{\partial \bar{V}}{\partial \rho} |_{(\rho_0, v_0)}$, $\bar{V}_v^0 = \frac{\partial \bar{V}}{\partial v} |_{(\rho_0, v_0)}$. Substituting Eqs. (20)–(24) into Eqs. (10) and (11), it can be derived that the coefficients of the first two terms ξ^0 and ξ^1 satisfy the following equations:

$$-\phi_0\rho_1 + \rho_0v_1 = 0 \tag{25}$$

$$\dot{\rho}_1 - \phi_0\rho_2 + \rho_0v_2 + 2\rho_1v_1 = 0 \tag{26}$$

$$\begin{aligned} -\phi_0v_1\rho_0^2 - a\rho_0^2\left(\gamma\bar{V}^0 - v_0\right) - a\gamma V_{e,\rho}^0\left(\frac{\rho_1\rho_0}{2} + \frac{\rho_2}{6}\right) \\ = 0 \end{aligned} \tag{27}$$

$$\begin{aligned} -\phi_0v_12\rho_0\rho_1 + (v_1 - \phi_0v_2)\rho_0^2 + \rho_0^2v_1^2 \\ - \left[a\gamma\bar{V}^02\rho_0\rho_1 + a\gamma\rho_0^2\left(\bar{V}_\rho^0\rho_1 + \bar{V}_v^0v_1\right) \right. \\ \left. - a(2\rho_0v_0\rho_1 + v_1\rho_0^2) \right] - a\gamma\left[\bar{V}_\rho^0\left(\frac{\rho_1^2 + \rho_2\rho_0}{2} + \frac{\rho_3}{6}\right) \right. \\ \left. + \left(\bar{V}_{\rho\rho}^0\rho_1 + \bar{V}_{\rho v}^0v_1\right)\left(\frac{\rho_1\rho_0}{2} + \frac{\rho_2}{6}\right) \right] = 0 \end{aligned} \tag{28}$$

where $\phi_0 = \pm \sqrt{-2a\gamma\bar{V}'(\rho_0)}/2$.

For Eqs. (26) and (28), we can derive the following determinant

$$\det \begin{vmatrix} -a\gamma \left(\frac{1}{2} \rho_0 \bar{V}_\rho^0 + \frac{1}{6} (\bar{V}_{\rho\rho}^0 \rho_1 + \bar{V}_{\rho v}^0 v_1) \right) & -\phi_0 \rho_0^2 \\ -\phi_0 & \rho_0 \end{vmatrix} = 0 \tag{29}$$

It indicates the coefficients of ρ_2 and v_2 are linearly dependent. Therefore, by eliminating ρ_2 and v_2 in Eqs. (26) and (28), the Bernoulli equation is obtained:

$$\dot{v}_1 + Cv_1 + Dv_1^2 = 0 \tag{30}$$

where $C = (2av_0 + a\phi_0 - 2a\gamma\bar{V}^0 - a\gamma\rho_0\bar{V}_\rho^0) / (2\phi_0)$, $D = (2\phi_0^2 - a\gamma\rho_0\bar{V}_{\rho\rho}^0 - a\gamma\bar{V}_\rho^0) / (4\phi_0^2)$, and $\bar{V}_v^0 = 0, \bar{V}_{\rho v}^0 = 0$. The slope of the points is along the wavefront trace. This equation specifies the slope evolution at the wavefront. The propagation stability defined by Eq. (30) can be analyzed in terms of the initial condition $v_1(0)$ and parameters C and D . The value of D is greater than zero for the two characteristic velocities. If $C = 0$, the solutions of the Bernoulli equation, Eq. (30), are

$$v_1(t) = \frac{v_1(0)}{Dv_1(0)t + 1} \tag{31}$$

Then, the monotonicity of function $v_1(t)$ is determined by the first derivative with respect to t :

$$\dot{v}_1(t) = -\frac{Dv_1^2(0)}{(Dv_1(0)t + 1)^2} \tag{32}$$

If $C \neq 0$, the general solutions of Eq. (30) can be specified as follows:

$$v_1(t) = \frac{C}{D} \frac{e^{-Ct}}{\left[1 + \frac{C}{Dv_1(0)} \right] - e^{-Ct}} \tag{33}$$

where $v_1(0)$ is determined by the initial condition for $v_1(t)$ at $t = 0$. Similar to the monotonicity of Eq. (31), the monotonicity of Eq. (33) is given by the first derivative with respect to t .

$$\dot{v}_1(t) = -\frac{C^2}{D} \frac{\left(1 + \frac{C}{Dv_1(0)} \right) e^{-Ct}}{\left\{ \left(1 + \frac{C}{Dv_1(0)} \right) - e^{-Ct} \right\}^2} \tag{34}$$

Therefore, the trend of $v_1(t)$ can be determined, as shown in Table 1. The stability conditions are listed in Table 1. When the density disturbance increases, the velocity perturbation decreases, specifically,

Table 1 Global stability conditions for the traffic flow according to Eq. (30) [52, 53]

Parameter C	Stable region	Unstable region
$C > 0$	$v_1(0) \in (-C/D, +\infty),$ $v_1(t) \rightarrow 0$	$v_1(0) \in (-\infty, -C/D),$ $v_1(t) \rightarrow -\infty$
$C = 0$	$v_1(0) \in R,$ $v_1(t) \rightarrow 0$	$v_1(0) \in (-\infty, 0),$ $v_1(t) \rightarrow -\infty$
$C < 0$	$v_1(0) \in (0, +\infty),$ $v_1(t) \rightarrow -C/D$	$v_1(0) \in (-\infty, 0),$ $v_1(t) \rightarrow -\infty$

$$C = (2av_0 + a\phi_0 - 2a\gamma\bar{V}^0 - a\gamma\rho_0\bar{V}_\rho^0) / (2\phi_0),$$

$$D = (2\phi_0^2 - a\gamma\rho_0\bar{V}_{\rho\rho}^0 - a\gamma\bar{V}_\rho^0) / (4\phi_0^2)$$

$v_1(0) < 0$. When $C > 0$, the first-order derivative $\dot{v}_1(t) < 0$ (due to $D > 0$). It indicates $v_1(t)$ is monotonic decreasing function, and tends to zero with time. Plugging it into Eq. (33), we can deduce $v_1(0) \in (-\frac{C}{D}, 0)$. The stability criterion for the traffic flow is:

$$C = \frac{2av_0 + a\phi_0 - 2a\gamma\bar{V}^0 - a\gamma\rho_0\bar{V}_\rho^0}{2\phi_0} > 0 \tag{35a}$$

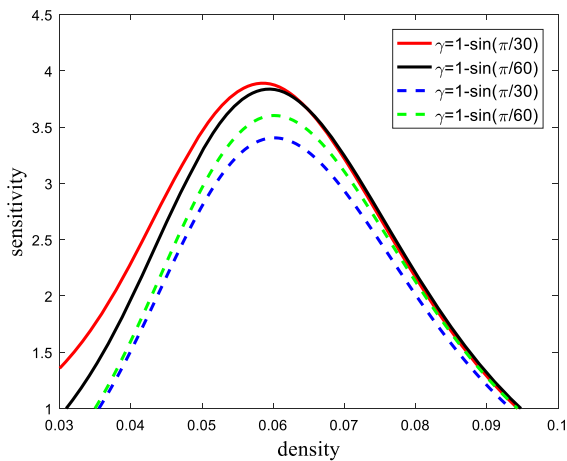
Thus, we can obtain the following expression:

$$\therefore v_0 = \bar{V}^0, \phi_0 = \pm \sqrt{-2a\gamma\bar{V}'(\rho_0)}/2$$

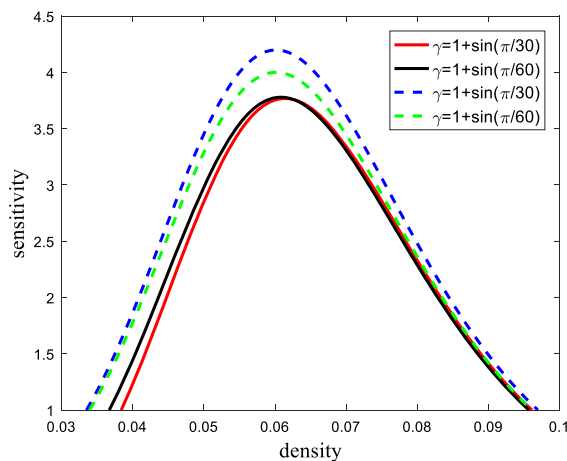
$$\therefore a > -2\gamma\rho_0^2\bar{V}_\rho^0 - 8(\gamma - 1)\bar{V}^0 \left[\rho_0 + \frac{(\gamma - 1)\bar{V}^0}{\gamma\bar{V}_\rho^0} \right] \tag{35b}$$

According to the comparison of the stability condition specified in Eq. (13), the stability criterion under large traffic disturbances is considerably different from the result of the linear analysis, which is followed by a term $-8(\gamma - 1)\bar{V}^0 \left[\rho_0 + \frac{(\gamma - 1)\bar{V}^0}{\gamma\bar{V}_\rho^0} \right]$. When $\theta = 0$ and $\gamma = 1$, Eq. (35b) can be expressed as $a > -2\rho_0^2\bar{V}_\rho^0$, which is the stability condition of the traffic flow on the flat road without considering the slope [52]. The model is stable against any initial condition as long as this stability criterion is satisfied.

In order to compare local stability (13) and global stability (35b), Fig. 2(a) and (b) shows the phase diagrams corresponding to different slope angles on the upslope and downslope, respectively, where the



(a) upslope



(b) downslope

Fig. 2 The phase diagram for different slope angles, and the solid line and dotted line, respectively, indicate global and local stability

equilibrium speed-density relationship $\bar{V}(\rho)$ proposed by Kerner et al. [65] is utilized. Local and global stability are represented by dashed and solid lines, respectively. The region under these curves is the region of instability. Under the action of small disturbance, with the increase of slope Angle, the local stability of upslope increases and the local stability of downslope decreases. Under large disturbance, the global stability also shows a similar insignificant effect, but the global instability region uphill is larger, while the global instability region downhill is smaller than the local instability region.

4 Hopf bifurcation

Considering the following nonlinear system:

$$\mathbf{x}' = f(\mathbf{x}, \chi), \mathbf{x} = (x_1 \ x_2)^T, \chi \subseteq R^2 \tag{36}$$

where f is a smooth function, and χ is a variable parameter. A linear equation around the origin is represented as $L(\chi) = D_x f(x, \chi)|_{(x_0)}$. It is assumed that the system has a pair of complex eigenvalues $\lambda_{1,2} = \alpha(\chi) \pm iw(\chi)$.

Lemma 1 Cao et al. [66]. *If the succeeding conditions are satisfied in the equilibrium state $\alpha(\chi_0) = 0, w(\chi_0) = w_0 > 0, c = \alpha'(\chi_0) \neq 0$, a Hopf bifurcation exists in the system when $\chi = \chi_0$.*

Lemma 2 Cao et al. [66]. *A dynamical system (36) with a smooth function f , for which χ is a variable parameter, exhibits equilibrium $x = 0$ with eigenvalues $\lambda_{1,2} = \alpha(\chi) \pm iw(\chi), \alpha(0) = 0, w(0) = w_0 > 0, c = \alpha'(0) \neq 0$. The following equation can be derived through a coordinate shift:*

$$\begin{cases} x'_1 = \alpha(\chi)x_1 - w(\chi)x_2 + \tilde{f}_1(x_1, x_2, \chi) \\ x'_2 = w(\chi)x_1 - \alpha(\chi)x_2 + \tilde{f}_2(x_1, x_2, \chi) \end{cases} \tag{37}$$

where $\tilde{f}_1, \tilde{f}_2 = o(x_1^2 + x_2^2)$. Subsequently, the first Lyapunov exponent of system (36) can be computed [66] as follows:

$$\begin{aligned} \varphi = (1/16) & [\tilde{f}_{1x_1x_1x_1} + \tilde{f}_{1x_1x_2x_2} + \tilde{f}_{2x_1x_1x_2} + \tilde{f}_{2x_2x_2x_2}]|_{(0,0,0)} \\ & + (1/16w_0) [\tilde{f}_{1x_1x_2}(\tilde{f}_{1x_1x_1} + \tilde{f}_{1x_2x_2}) - \tilde{f}_{2x_1x_2}(\tilde{f}_{2x_1x_1} + \tilde{f}_{2x_2x_2}) \\ & - \tilde{f}_{1x_1x_1x_1}\tilde{f}_{2x_1x_1} + \tilde{f}_{1x_2x_2x_2}\tilde{f}_{2x_2x_2}]|_{(0,0,0)} \end{aligned} \tag{38}$$

If $\varphi < 0$ and $c > 0$, the Hopf bifurcation is supercritical, and if $\varphi > 0$ and $c > 0$, the Hopf bifurcation is subcritical [66].

For the dynamical system (36), we perform the following coordinate shift to change the reference system.

$$z = x - ct \tag{39}$$

where c is the constant velocity of the moving coordinate system with respect to the stationary coordinate system. Substituting Eq. (39) into Eq. (10) yields

$$\rho(v - c) = q_* \tag{40}$$

where q_* is a constant. Substituting Eqs. (39) and (40) into Eq. (11) yields the following equation:

$$\frac{a\gamma\bar{V}'(\rho)}{6\rho}\rho_{zz} + \left[\frac{1}{2}a\gamma\bar{V}'(\rho) + \frac{q_*^2}{\rho^2}\right]\rho_z + a(\gamma\rho\bar{V}(\rho) - (q_* + \rho c)) = 0 \tag{41}$$

Equation (41) can be reformulated as follows:

$$\rho_{zz} - G(\rho, q_*)\rho_z - F(\rho, c, q_*) = 0 \tag{42}$$

where $G(\rho, q_*) = -\frac{3a\gamma\rho^2\bar{V}'(\rho)+6q_*^2}{a\gamma\rho\bar{V}'(\rho)}$, $F(\rho, c, q_*) = -\frac{6\rho(\gamma\rho\bar{V}(\rho)-(q_*+\rho c))}{\gamma\bar{V}'(\rho)}$. This equation can be converted into the equation group

$$\begin{cases} d\rho/dz = y \\ dy/dz = G(\rho, q_*)y + F(\rho, c, q_*) \end{cases} \tag{43}$$

Let $(\rho_i, 0)$ represent the equilibrium point of Eq. (43). The equilibrium point can be determined by assuming that the right-hand term of Eq. (43) is zero, that is, $y = 0$ and $F(\rho, c, q_*) = 0$. The Taylor expansion of the right-hand term of the second equation of equation group (43) at the equilibrium point can be obtained:

$$\begin{cases} \rho' = y \\ y' = G(\rho_i, q_*)y + F'(\rho_i, c, q_*)(\rho - \rho_i) \end{cases} \tag{44}$$

where $F'(\rho_i, c, q_*) = -6\rho_i[\gamma\bar{V}'(\rho_i) + \gamma\rho_i - \bar{V}'(\rho_i) - c]/(\gamma\bar{V}'(\rho_i))$. At equilibrium point $F(\rho, c, q_*) = 0, \gamma\rho_i\bar{V}(\rho_i) - (q_* + \rho_i c) = 0$ with $F'_i(\rho_i, c, q_*) = -6(q_* + \gamma\rho_i^2\bar{V}'(\rho_i))/(\gamma\bar{V}'(\rho_i))$. The Jacobian characteristic equation of Eq. (44) at the equilibrium point $(\rho_i, 0)$ can be obtained as

$$\mathbf{L} = \begin{pmatrix} 0 & 1 \\ F'_i & G_i \end{pmatrix} = \begin{pmatrix} 0 & 1 \\ b(q_*) & d(q_*) \end{pmatrix} \tag{45}$$

where $G_i = G(\rho_i, q_*)$, $F'_i = F'(\rho_i, c, q_*)$. The characteristic equation of Eq. (45) is defined as $\lambda^2 - \sigma\lambda + \Delta = 0$, where $\sigma = d(q_*) = \text{trace}(\mathbf{L})$, $\Delta = -b(q_*) = \det(\mathbf{L})$. Assuming the matrix \mathbf{L} has eigenvalues $\lambda = \alpha(q_*) \pm iw(q_*)$, the eigenvalue solutions to the above characteristic equation can be specified as

$$\lambda_{1,2} = \frac{\sigma(q_*) \pm \sqrt{\sigma(q_*)^2 - 4\Delta(q_*)}}{2} \tag{46}$$

The following variable transformation is performed,

$$\alpha(q_*) = \frac{1}{2}\sigma(q_*), \quad w(q_*) = \sqrt{\Delta(q_*) - \frac{\sigma^2(q_*)}{4}} \tag{47}$$

and Lemma 1 is considered to obtain

$$c = \alpha'(q_*) = -\frac{6q_*}{a\gamma\rho_0\bar{V}'(\rho_0)} \tag{48}$$

where $q_* = q_{*0}$ at the equilibrium point $(\rho_0, 0) = (\rho_i, 0)$. Thus, the Hopf bifurcation exists according to Lemma 1 when the following equation is satisfied:

$$\alpha(q_{*0}) = 0, w(q_{*0}) = w_0 > 0, c = \alpha'(q_{*0}) \neq 0 \tag{49}$$

Specifically,

$$q_{*0} = \sqrt{-a\gamma\rho_0^2\bar{V}'(\rho_0)}/2, q_{*0} + \gamma\rho_0^2\bar{V}'(\rho_0) < 0, \lambda_{1,2} = \pm iw_0 \tag{50}$$

Next, we examine the type of Hopf bifurcation of the system. The eigenvector of $\mathbf{L}(q_*)$ is assumed to be $w_{re} + iw_{im}$, and according to Eq. (49), the value can be obtained as follows:

$$\mathbf{L}(w_{re} + iw_{im}) = iw_0(w_{re} + iw_{im}) \tag{51}$$

The real and imaginary parts of Eq. (51) are equal.

$$\mathbf{L}w_{im} = w_0w_{re}, \mathbf{L}w_{re} = -w_0w_{im} \tag{52}$$

The matrix form is

$$\mathbf{L} \begin{bmatrix} w_{im} & w_{re} \end{bmatrix} = \begin{bmatrix} w_{im} & w_{re} \end{bmatrix} \begin{bmatrix} 0 & -w_0 \\ w_0 & 0 \end{bmatrix} \tag{53}$$

The transpose of the matrix can be obtained as

$$\begin{bmatrix} w_{im} & w_{re} \end{bmatrix}^{-1} \mathbf{L} \begin{bmatrix} w_{im} & w_{re} \end{bmatrix} = \begin{bmatrix} 0 & -w_0 \\ w_0 & 0 \end{bmatrix} \tag{54}$$

Let

$$\tilde{y} = \begin{bmatrix} w_{im} & w_{re} \end{bmatrix}^{-1} \tilde{x} \tag{55}$$

we can obtain

$$\tilde{y}' = \begin{bmatrix} w_{im} & w_{re} \end{bmatrix}^{-1} \tilde{x}' \tag{56}$$

For Eq. (43), the coordinate shift is performed, assuming $\tilde{\rho} = \rho - \rho_0$. In particular, the equilibrium point translates to the origin, and we obtain

$$\begin{cases} \tilde{\rho}' = y \\ y' = -\frac{3a\gamma(\tilde{\rho} + \rho_0)^2\bar{V}'(\tilde{\rho} + \rho_0) + 6q_{*0}^2}{a\gamma(\tilde{\rho} + \rho_0)\bar{V}'(\tilde{\rho} + \rho_0)}y \\ \quad - \frac{6a(\tilde{\rho} + \rho_0)(\gamma(\tilde{\rho} + \rho_0)\bar{V}'(\tilde{\rho} + \rho_0) - (q_* + (\tilde{\rho} + \rho_0)c))}{a\gamma\bar{V}'(\tilde{\rho} + \rho_0)} \end{cases} \tag{57}$$

This equation is linearized at the original point by the Taylor expansion $(\tilde{\rho}, y) = (0, 0)$. In other words,

$$\tilde{x}' = \mathbf{L}(q_*)\tilde{x} + f \tag{58}$$

where

$$f = \begin{bmatrix} 0 \\ k_{11}\tilde{\rho}^2 + k_{22}y^2 + k_{12}\tilde{\rho}y + k_{111}\tilde{\rho}^3 + k_{222}y^3 + k_{112}\tilde{\rho}^2y + k_{122}\tilde{\rho}y^2 + o(\tilde{\rho}, y)^4 \end{bmatrix} \tag{59}$$

Substituting Eqs. (55) and (58) into Eq. (56) yields

$$\begin{aligned} \tilde{y}' &= [w_{im} \ w_{re}]^{-1}\mathbf{L}[w_{im} \ w_{re}]\tilde{y} + [w_{im} \ w_{re}]^{-1}f \\ &= \begin{bmatrix} 0 & -w_0 \\ w_0 & 0 \end{bmatrix}\tilde{y} + [w_{im} \ w_{re}]^{-1}f \end{aligned} \tag{60}$$

The eigenvector of $\mathbf{L}(q_*)$ can be represented as

$$w_{re} + iw_{im} = \begin{pmatrix} 0 \\ 1 \end{pmatrix} + i \begin{pmatrix} -\frac{1}{\sqrt{-F'}} \\ 0 \end{pmatrix} \tag{61}$$

Substituting Eq. (59) into Eq. (60) yields

$$\begin{aligned} \tilde{y}' &= \begin{bmatrix} 0 & -w_0 \\ w_0 & 0 \end{bmatrix}\tilde{y} \\ &\quad + [w_{im} \ w_{re}]^{-1} \begin{bmatrix} 0 \\ k_{11}\tilde{\rho}^2 + k_{22}y^2 + k_{12}\tilde{\rho}y + k_{111}\tilde{\rho}^3 + k_{222}y^3 + k_{112}\tilde{\rho}^2y + k_{122}\tilde{\rho}y^2 + o(\tilde{\rho}, y)^4 \end{bmatrix} \end{aligned} \tag{62}$$

In this case, the first Lyapunov coefficient is [62]

$$\varphi = \frac{1}{16} \left(\tilde{f}_{2\tilde{y}_1\tilde{y}_1\tilde{y}_2} + \tilde{f}_{2\tilde{y}_2\tilde{y}_2\tilde{y}_2} \right) \Big|_{(0,0,q_{*0})} - \frac{1}{16w_0} \left[\tilde{f}_{2\tilde{y}_1\tilde{y}_2} \left(\tilde{f}_{2\tilde{y}_1\tilde{y}_1} + \tilde{f}_{2\tilde{y}_2\tilde{y}_2} \right) \right] \Big|_{(0,0,q_{*0})} \tag{63}$$

Notably,

$$\begin{aligned} c = \alpha'(0) &= -\frac{6q_{*0}}{a\gamma\rho\bar{V}'(\rho)} \\ &= -\frac{6q_{*0}}{a(1 \mp \sin\theta)\rho\bar{V}'(\rho)} > 0 \end{aligned} \tag{64}$$

When $\varphi < 0$, the Hopf bifurcation of the model is a supercritical bifurcation, and the limit cycle formed by the supercritical bifurcation is stable. If $\varphi > 0$, the Hopf bifurcation is a subcritical bifurcation [66].

Lemma 3 [66]. Assumed \mathbf{L} has a single zero eigenvalue and the other eigenvalues are non-zero real parts, when $\xi_1 = \psi D_\chi f(x, \chi)|_{(x_0, \chi_0)} \neq 0$, $\xi_2 = \psi D_x D_\chi f(x, \chi)|_{(x_0, \chi_0)}(\zeta, \zeta) \neq 0$ where $L\zeta = 0, \psi L = 0$, exists saddle-node bifurcation in $\chi = \chi_0$.

For system (43), when

$$q_{*0} + \gamma\rho_0^2 V'_e(\rho_0) = 0 \tag{65}$$

The vectors

$$\psi = \begin{pmatrix} \frac{3a\gamma\rho_0^2\bar{V}'(\rho_0) + 6q_{*0}^2}{a\gamma\rho_0\bar{V}'(\rho_0)} & 1 \end{pmatrix} \zeta = \begin{pmatrix} 1 \\ 0 \end{pmatrix} \text{ satisfy}$$

$L\zeta = 0, \psi L = 0$. Thus,

$$\begin{aligned} \xi_1 &= \psi \cdot \frac{\partial}{\partial q_*} f(x, q_*)|_{(x_0, q_{*0})} \\ &= \begin{pmatrix} \frac{3a\gamma\rho_0^2\bar{V}'(\rho_0) + 6q_{*0}^2}{a\gamma\rho_0\bar{V}'(\rho_0)} & 1 \end{pmatrix} \begin{pmatrix} 0 \\ \frac{6\rho_0}{\gamma\bar{V}'(\rho_0)} \end{pmatrix} \\ &= \frac{6\rho_0}{\gamma\bar{V}'(\rho_0)} \neq 0 \end{aligned} \tag{66}$$

$$\begin{aligned} \xi_2 &= \psi D_x D_x f(x, \chi)|_{(x_0, \zeta_0)}(\zeta, \zeta) \\ &= \left(\frac{3a\gamma\rho_0^2 \bar{V}'(\rho_0) + 6q_*^2}{a\gamma\rho_0 \bar{V}'(\rho_0)} 1 \right) \cdot \begin{pmatrix} [1 \ 0] \begin{bmatrix} 0 & 0 \\ 0 & 0 \end{bmatrix} \begin{bmatrix} 1 \\ 0 \end{bmatrix} \\ [1 \ 0] \begin{bmatrix} A_1 & A_2 \\ A_2 & 0 \end{bmatrix} \begin{bmatrix} 1 \\ 0 \end{bmatrix} \end{pmatrix} = A_1 \neq 0 \end{aligned} \tag{67}$$

where

$$\begin{aligned} A_1 &= - \frac{12[\gamma\bar{V}(\rho_0) + 2\gamma\rho_0\bar{V}'(\rho_0) - c] + 6\gamma\rho_0^2\bar{V}''(\rho_0)}{\gamma\bar{V}'(\rho_0)} \\ A_2 &= - \frac{[3a\gamma\rho_0^2\bar{V}'(\rho_0) + 6q_*^2][\bar{V}'(\rho_0) + \rho_0\bar{V}''(\rho_0)]}{a\gamma[\rho_0\bar{V}'(\rho_0)]^2} \\ &\quad - \frac{[6\bar{V}'(\rho_0) + 3\rho_0\bar{V}''(\rho_0)]}{\bar{V}'(\rho_0)} \end{aligned}$$

Thus, a saddle-node bifurcation exists in system (43) at $q_* = q_{*0} = -\gamma\rho_0^2 V'_e(\rho_0)$.

5 Numerical simulations

We study the spatiotemporal evolution of traffic density waves under no-flux boundary conditions. The traffic flow uphill, downhill and continuous uphill and downhill is simulated. To study the local cluster effect induced by a localized perturbation in an initial homogeneous condition, we use the finite difference method to discretize Eqs. (10) and (11). To discretize the conservation equation, Eq. (10), and motion equation, Eq. (11), we use the first-order upwind scheme to discretize the macroscopic equation that can be adapted to the physical meaning of the traffic flow to obtain:

$$\rho_j^{i+1} = \rho_j^i + \frac{\Delta t}{\Delta x} \rho_j^i (v_j^i - v_{j+1}^i) + \frac{\Delta t}{\Delta x} v_j^i (\rho_{j-1}^i - \rho_j^i) \tag{68}$$

$$\begin{aligned} v_j^{i+1} &= v_j^i - \Delta t v_j^i \frac{v_j^i - v_{j-1}^i}{\Delta x} + a\Delta t [\gamma\bar{V}(\rho_j^i) - v_j^i] \\ &\quad + a\gamma\bar{V}'(\rho) \Delta t \left[\frac{\rho_{j+1}^i - \rho_j^i}{2\rho_j^i \Delta x} + \frac{\rho_{j+1}^i - 2\rho_j^i + \rho_{j-1}^i}{6(\rho_j^i)^2 (\Delta x)^2} \right] \end{aligned} \tag{69}$$

The related parameters are as follows:

$$a = 0.2s^{-1}, \quad L = 32.2\text{km}, \quad \Delta x = 100\text{m}, \quad \Delta t = 1\text{s}$$

$$\rho_m = 0.2\text{veh/m}, \quad v_f = 30\text{m/s}$$

where L denotes the length of all roads, Δx and Δt are the space interval and time interval, respectively, and ρ_m represents the maximum density or jam density.

The initial density is expressed as the following density function, proposed by Herrmann and Kerner [67]:

$$\begin{aligned} \rho(x, 0) &= \rho_0 + \Delta\rho_0 \left\{ \cosh^{-2} \left[\frac{160}{L} \left(x - \frac{5L}{16} \right) \right] \right. \\ &\quad \left. - \frac{1}{4} \cosh^{-2} \left[\frac{40}{L} \left(x - \frac{11L}{32} \right) \right] \right\} \end{aligned} \tag{70}$$

where $\Delta\rho_0$ is the density fluctuation, with $\Delta\rho_0 = 10^{-2}\text{veh/m}$.

The equilibrium speed–density relationship [65] is selected as follows:

$$\bar{V}(\rho) = v_f \left[\left(1 + \exp \frac{\rho/\rho_m - 0.25}{0.06} \right)^{-1} - 3.72 \times 10^{-6} \right] \tag{71}$$

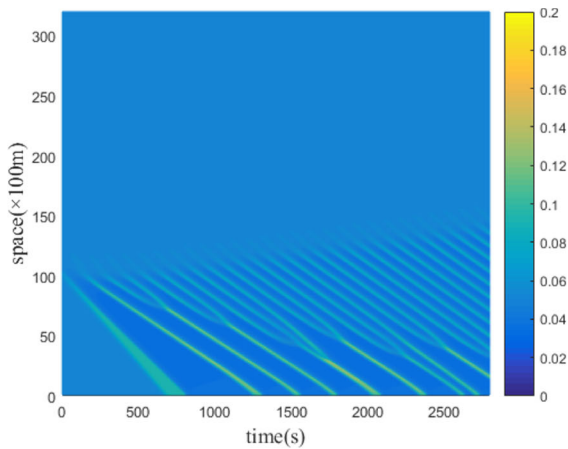
According to the global stability analysis, the critical density is obtained by substituting the above parameter into Eq. (35b):

$$\begin{aligned} \rho_{c1} = 0.0304 \leq \rho_0 \leq 0.1217 = \rho_{c2}, \quad \gamma = 1 + \sin(\pi/30) \\ \rho_{c1} = 0.0274 \leq \rho_0 \leq 0.1213 = \rho_{c2}, \quad \gamma = 1 + \sin(\pi/60) \\ \rho_{c1} = 0.0223 \leq \rho_0 \leq 0.1208 = \rho_{c2}, \quad \gamma = 1 \\ \rho_{c1} = 0.0 \leq \rho_0 \leq 0.1198 = \rho_{c2}, \quad \gamma = 1 - \sin(\pi/30) \\ \rho_{c1} = 0.0 \leq \rho_0 \leq 0.1203 = \rho_{c2}, \quad \gamma = 1 - \sin(\pi/60) \end{aligned} \tag{72}$$

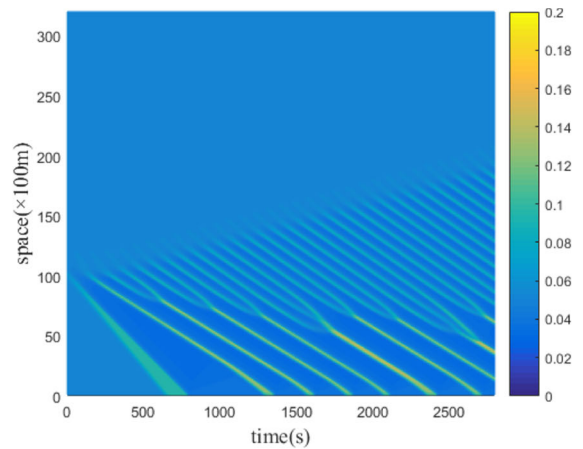
where $\rho_0 \in [0, \rho_m]$, the global instability region lies between the upper critical density and the lower critical density [14, 54].

5.1 Evolution of the traffic flow on the upslope or downslope

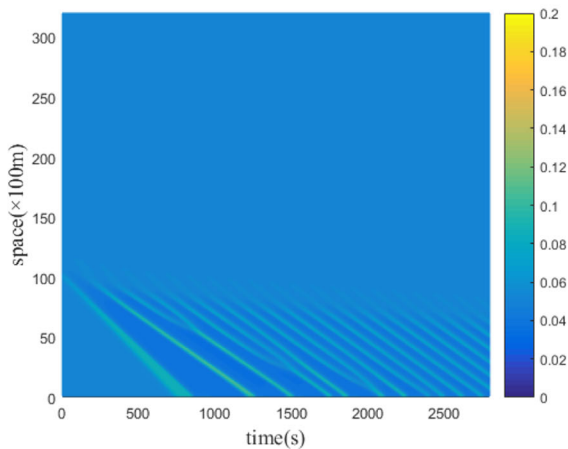
First, we perform a simulation for the spatiotemporal pattern of the traffic density on the upslope or downslope. Figures 3 and 4 display the spatiotemporal evolution patterns of the density waves on the upslope and downslope when the initial density is $\rho_0 = 0.053\text{veh/m}$, respectively. Figure 3a and b shows that the density wave is attenuated as the slope angle increases from $\theta_1 = \pi/60$ to $\theta_1 = \pi/15$, consistent with the stable condition specified in Eq. (14) for the upslope. Figure 4a and b shows that the density



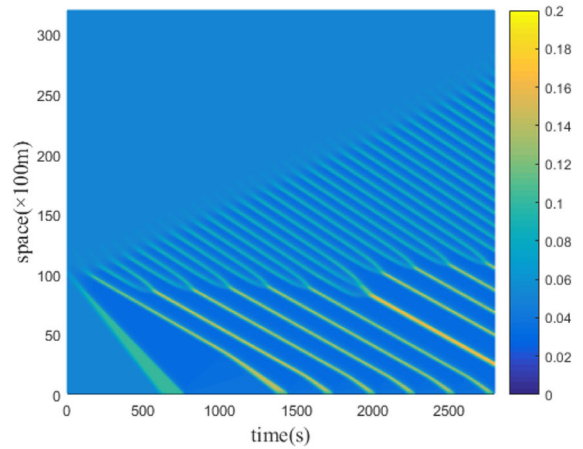
(a) $\theta_1 = \pi/60$



(a) $\theta_2 = \pi/60$



(b) $\theta_1 = \pi/15$



(b) $\theta_2 = \pi/15$

Fig. 3 Spatiotemporal density pattern of traffic flow on the upslope

wave intensifies as the slope angle increases from $\theta_2 = \pi/60$ to $\theta_2 = \pi/15$. In the case of downhill slopes, the traffic stability decreases with increasing slope angle, which agrees with the criterion specified in Eq. (15) for the downhill stability condition.

5.2 Evolution of traffic flow on the upslope and downslope

Figure 5a–c shows the spatiotemporal density patterns of traffic flow on the upslope and downslope for different initial density ρ_0 . Under the condition of slope Angle $\theta_1 = \pi/90$ and $\theta_2 = \pi/90$, no matter the

Fig. 4 Spatiotemporal density pattern of traffic flow on the downslope

class of road is upslope or downslope, the traffic system is in a global stable state when the initial density is less than 0.01 and greater than 0.12. When the initial density is smaller than the lower critical density ρ_{c1} , the disturbance decays rapidly over time. When the value of the initial density lies between the lower and upper critical densities, two or more clusters of dipole-like structures are formed. When the initial density exceeds the upper critical density ρ_{c2} , the disturbance decays and a stable region is generated. This finding is consistent with Gupta’s results [54]. Two types of disturbance waves can be observed propagating forward and backward. Notably, the forward-propagating waves decay rapidly, in agreement with the observations of Yi et al. [52].

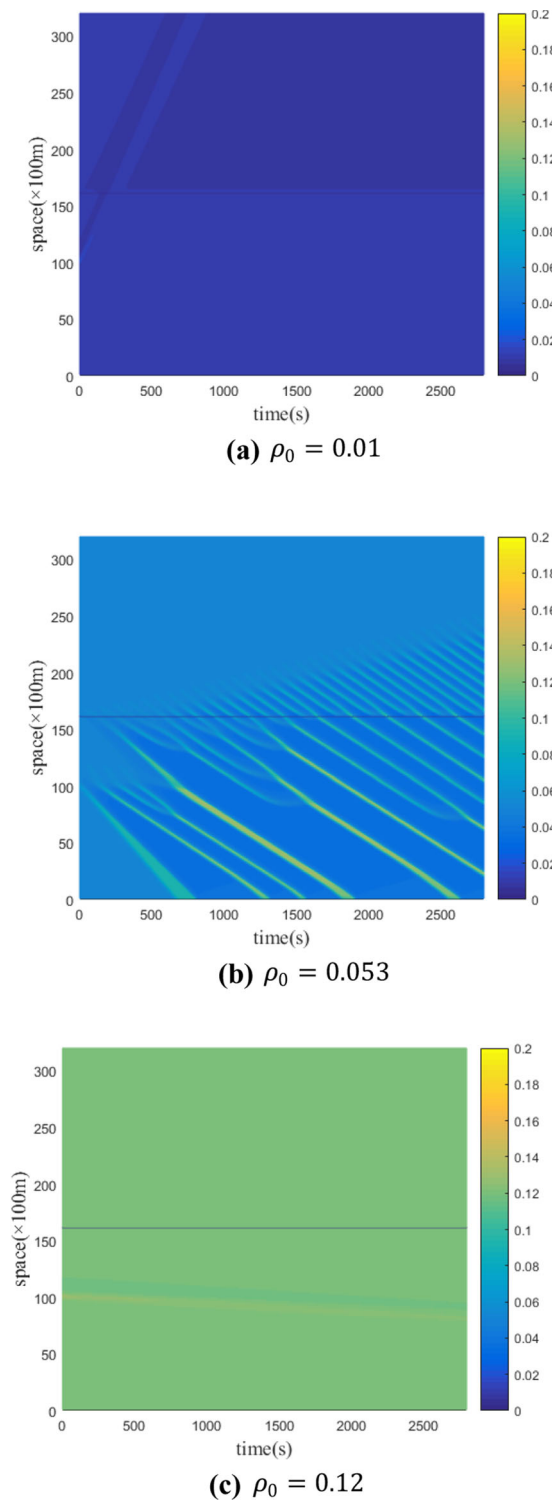


Fig. 5 Spatiotemporal density pattern of traffic flow for different initial densities on the upslope and downslope ($\theta_1 = \pi/90, \theta_2 = \pi/90$)

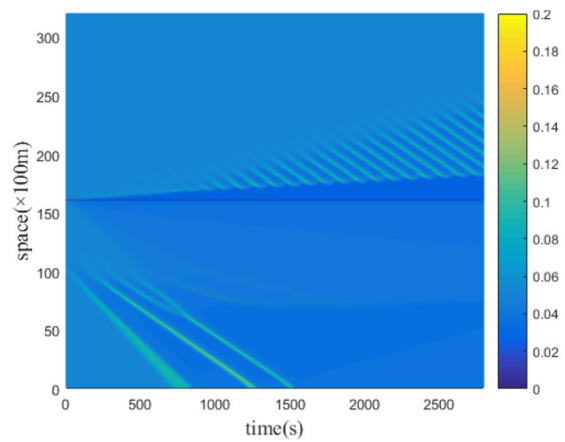
Figure 6a–c shows the evolution pattern of the density wave when the initial condition $\rho_0 = 0.053$ veh/m and the upslope and downslope angles change. Consider a situation in which the length of the upslope and downslope is $L/2$. When both the upslope and downslope are considered, increasing the upslope or downslope angle reduces the density fluctuation propagating downstream. Increasing only the slope angle can help enhance the stability.

Figure 7a and b shows the spatiotemporal density patterns when the initial condition $\rho_0 = 0.053$ veh/m, and the length of the upslope and downslope changes. The upslope length is L_1 , and the downslope length is L_2 . Comparison of Fig. 7a and b with Fig. 6a shows that when the uphill length is smaller than the downhill length at the same angle, the cluster size decreases, and the clusters become smoother downstream of the traffic flow. The density waves of traffic are more stable downstream (upslope situation) of the traffic flow, reflecting the influence of the slope length on the traffic flow stability.

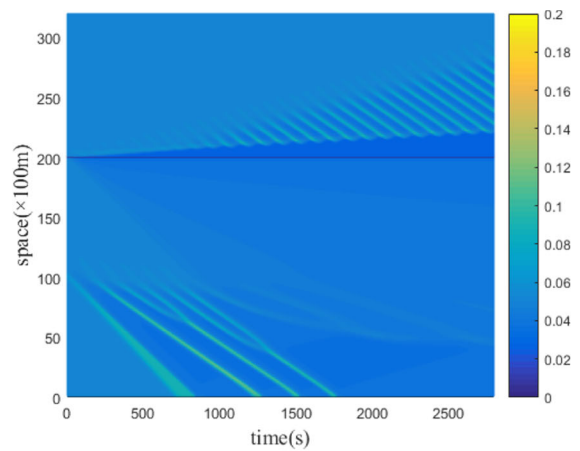
5.3 Saddle-node bifurcation and Hopf bifurcation

As described in this section, a numerical simulation is performed to study the bifurcation characteristics of uphill and downhill traffic flows. The parameters $(c, q_*) = (-1.371, 0.2)$ [62] selected to derive the equilibrium point specified in Sect. 5 are summarized in Table 2. According to the nonlinear stability theory, the stability of the equilibrium point is confirmed. As shown in Fig. 8a, when the disturbance is around the equilibrium point, only the equilibrium point ρ_2 remains stable, in accordance with the theoretical results. Figure 8b shows that the right shift of the equilibrium point ρ_2 with decreasing Angle of upslope. Conversely, as the Angle of downslope increases, the equilibrium point ρ_2 shifts to the right. Taking the equilibrium point $(\rho_2, 0)$ as the initial point, and the variable parameter q_* is selected as 0.2 at the initial moment.

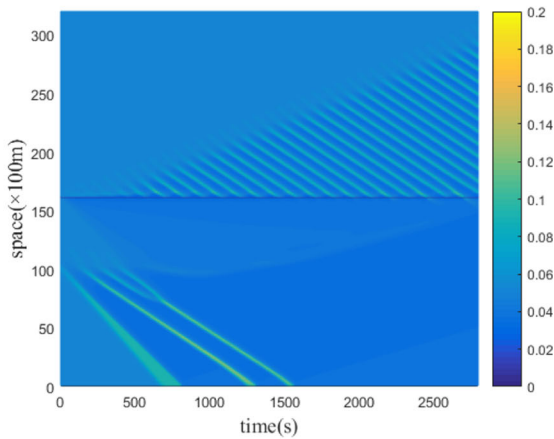
Using the package MATCONT of MATLAB, the location of the Hopf bifurcation point can be obtained in phase space as shown in Table 3. Substituting the density of Hopf bifurcation point into the Eq. (50), it is found that the existence condition of Hopf bifurcation is satisfied, which is consistent with the theoretical analysis. Figure 9a displays the bifurcation diagram of $\rho - q_*$ of the Angle parameter $\gamma = 1 + \sin(\pi/60)$.



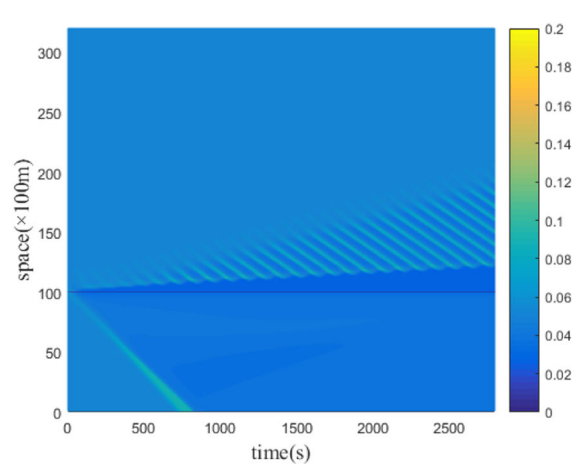
(a) $\theta_1 = \pi/20; \theta_2 = \pi/60$



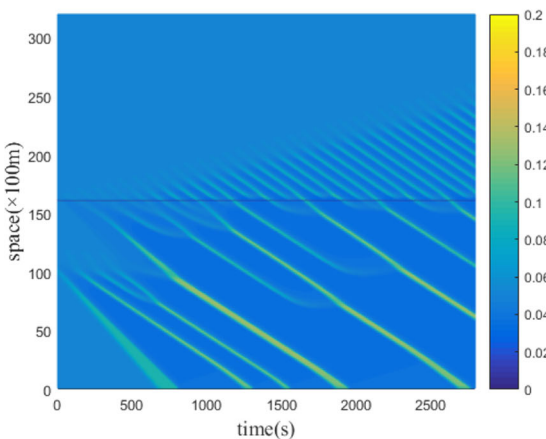
(a) $L_1 = 200 \text{ km}, L_2 = 122 \text{ km}$



(b) $\theta_1 = \pi/60; \theta_2 = \pi/20$



(b) $L_1 = 100 \text{ km}, L_2 = 222 \text{ km}$



(c) $\theta_1 = \pi/60; \theta_2 = \pi/60$

Fig. 6 Spatiotemporal density patterns obtained by changing the angle of the slope, considering both the upslope and downslope

Fig. 7 Spatiotemporal density patterns for different upslope and downslope lengths when both the upslope and downslope are considered. ($\theta_1 = \pi/20; \theta_2 = \pi/60$)

There exist two types of bifurcation: one is Hopf bifurcation (H) at $(q_*, \rho) = (0.3961, 0.07297)$, the other is limit point bifurcation (LP) at $(q_*, \rho) = (0.93544, 0.04063)$. Plugging in Eq. (65): $\gamma \rho_0^2 V_e'(\rho_0) = 0.9357$, the existence condition of saddle-node bifurcation can be obtained. When the Angle parameter $\gamma = 1 - \sin(\pi/60)$, Fig. 9b shows the Hopf bifurcation (H) at $(q_*, \rho) = (0.3829, 0.07187)$, and the limit point bifurcation at $(q_*, \rho) = (0.84795, 0.04071)$. Plugging in the Eq. (65): $\gamma \rho_0^2 V_e'(\rho_0) = 0.8479$, the existence condition of saddle-node bifurcation is satisfied. According to Eq. (63), the first Lyapunov coefficient ϕ can be calculated. Table 3 lists all Hopf

Table 2 Types and stabilities of several equilibrium points determined using the model parameters $\Delta_i = G_i^2 + 4F_i^2, i = 1, 2, 3, (c, q_*) = (-1.371, 0.2), a = 0.2$ [62, 66]

γ	$\rho_1(F'_i > 0, \text{ saddle point unstable for } z \rightarrow +\infty)$	$\rho_2(\Delta_i < 0, G_i < 0, \text{ spiral point stable for } z \rightarrow +\infty, \text{ unstable for } z \rightarrow -\infty)$	$\rho_3(F'_i > 0, \text{ saddle point unstable for } z \rightarrow +\infty)$
$1 - \sin(\pi/30)$	0.0074	0.0918	0.1449
$1 - \sin(\pi/60)$	0.0070	0.0928	0.1449
1	0.0066	0.0939	0.1449
$1 + \sin(\pi/60)$	0.0063	0.0949	0.1447
$1 + \sin(\pi/30)$	0.0060	0.0958	0.1447

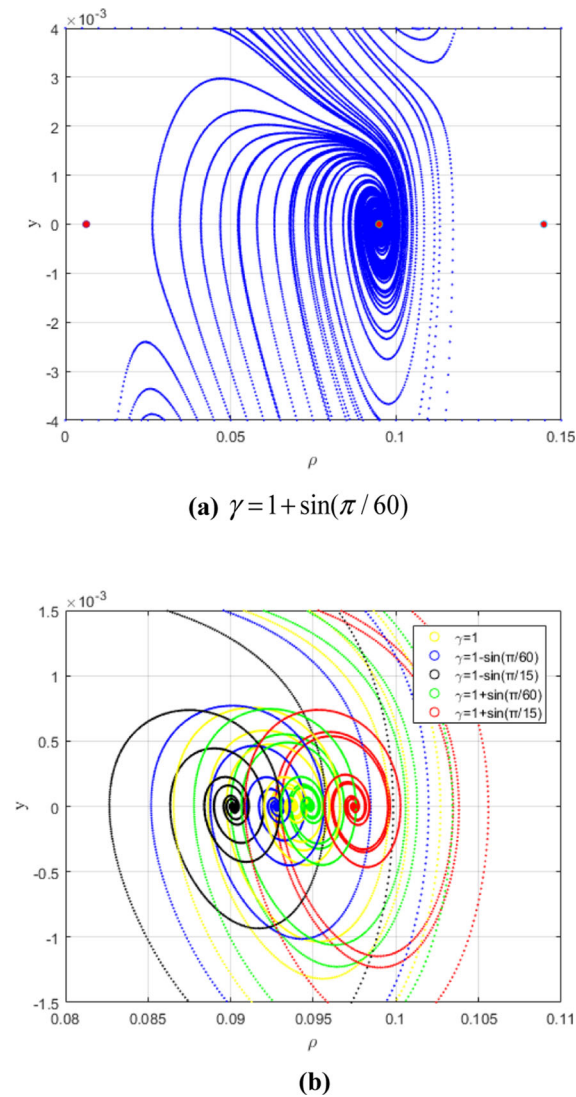


Fig. 8 Trajectories in the $\rho - y$ phase with different slope coefficients $((c, q_*) = (-1.371, 0.2))$

bifurcation points and the first Lyapunov coefficient φ for different slope angles on the upslope and downslope. The phase diagram shown as Fig.10a and b is obtained near the Hopf bifurcation point. According to the trajectory, the system has a stable focus and an unstable limit cycle.

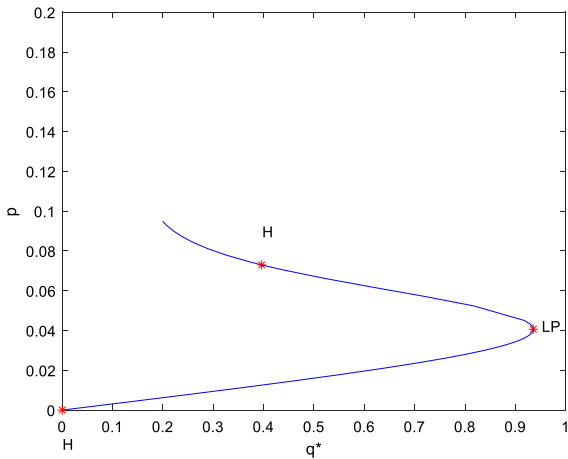
As can be seen from Table 3, the first Lyapunov coefficient φ is greater than zero. This indicates that the Hopf bifurcation is a subcritical bifurcation. Many studies have shown that the bifurcation structure is related to traffic congestion through the transformation of traveling waves. Igarashi believes the bifurcation point determines the boundary of different traffic state in the fundamental diagram [68]. The uniform flow equilibrium of the traffic system loses its stability because of Hopf bifurcations [60]. Table 3 and (72) indicate that the direction of the Hopf bifurcation moving with the slope Angle is consistent with the critical density of global stability, and the density at Hopf bifurcation point is between the upper critical density and the lower critical density. It means that the bifurcation causes instability in the traffic system.

6 Conclusion

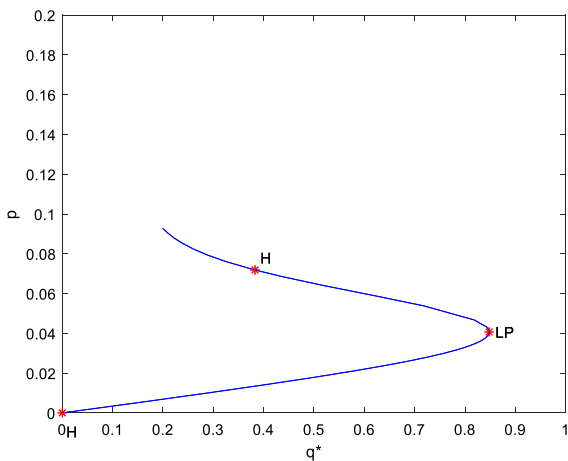
We derive a macro-continuum model of traffic flow from a microscale car-following model considering both upslope and downslope by using the transformation relationship between macro- and micro-variables. The perturbation propagation characteristics and stability conditions of the macroscopic continuum equation are discussed. Although the continuum equation has isotropic characteristics, the forward propagation characteristic velocity promptly decays and does not affect the vehicle in front. For the uniform flow in the

Table 3 The Hopf bifurcation point and first Lyapunov coefficient

Angle parameter γ	Hopf bifurcation point	First Lyapunov coefficient φ
$\gamma = 1 + \sin(\pi/30)$	$(q_*, \rho) = (0.4022, 0.07348)$	2.6637
$\gamma = 1 + \sin(\pi/60)$	$(q_*, \rho) = (0.3961, 0.07297)$	3.0686
$\gamma = 1$	$(q_*, \rho) = (0.3897, 0.07243)$	3.5019
$\gamma = 1 - \sin(\pi/30)$	$(q_*, \rho) = (0.3757, 0.07128)$	4.4613
$\gamma = 1 - \sin(\pi/60)$	$(q_*, \rho) = (0.3829, 0.07187)$	3.9655



(a) $\gamma = 1 + \sin(\pi / 60)$



(b) $\gamma = 1 - \sin(\pi / 60)$

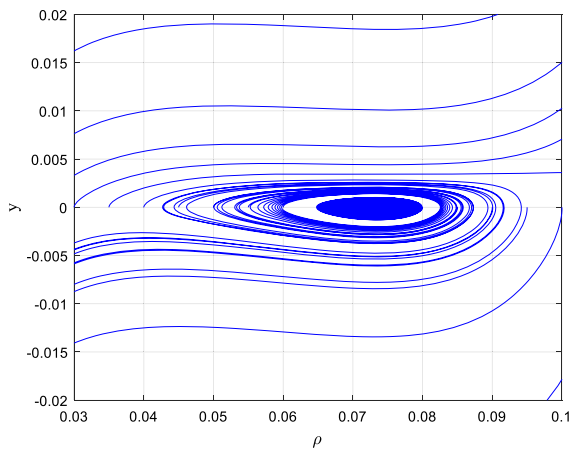
Fig. 9 The bifurcation diagram of $\rho - q_*$

initial equilibrium state, the stability conditions show that the upslope stability increases with increasing slope angle, and the downslope stability decreases with increasing slope angle under the action of a small disturbance. Under a large disturbance, the global

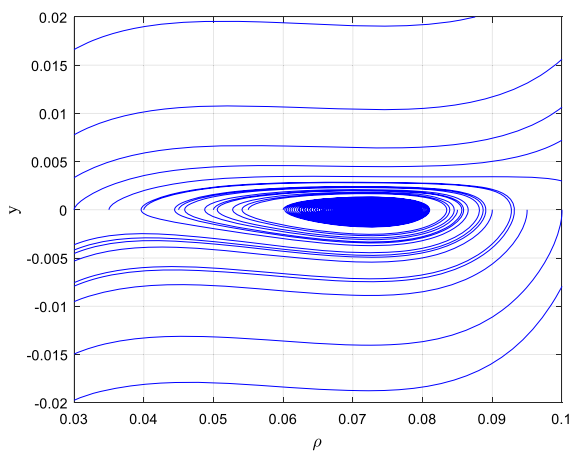
stability criterion is derived using the wave front expansion technique for uniform flow in the initial equilibrium state. The upslope global stability condition is different from that in the downslope condition. For the nonuniform flow in the initial non-equilibrium state, we perform a bifurcation analysis of the traffic flow at the equilibrium point. The results illustrate that a subcritical Hopf bifurcation exists when the traffic flow state changes. The limit cycle formed by Hopf bifurcation is unstable. Meanwhile, the existence condition of saddle node bifurcation is deduced by theoretical analysis.

Simulation results verify the stability conditions of the model. The critical density range is determined. The forward propagation disturbance decreases rapidly when the characteristic velocity is larger than the traffic flow velocity. The Hopf bifurcation and saddle-node bifurcation with different slope Angle in phase space is verified via numerical simulations. The corresponding bifurcation diagram is displayed. Furthermore, the impact of the angle of both the upslope and downslope on the evolution of density waves is studied. The amplitude of the density wave decreases with increasing ascending slope angle or decreasing descending slope angle, and the length of the slope exerts a certain influence on the traffic density wave. For a given slope angle, the clusters become smaller and smoother downstream of the traffic flow when the upslope length is smaller than the downslope length.

It is of practical significance to study the nonlinear behavior of traffic congestion formation and dissipation caused by road constraints. Road traffic bottlenecks such as road reduction, on-ramp, etc., are prone to traffic congestion. And the bifurcation structure is related to traffic congestion through the change of traveling waves. The research method of this paper can be widely extended to the bifurcation phenomenon induced by various traffic bottlenecks, and the overall stability of traffic at road bottlenecks and the formation mechanism of bifurcation phenomenon can be



(a) $\gamma = 1 + \sin(\pi / 60), q_* = 0.390$



(b) $\gamma = 1 - \sin(\pi / 60), q_* = 0.375$

Fig. 10 The Hopf bifurcation with different slope Angle

discussed. This will be the subject of our further research in the future.

Acknowledgements This work is supported by the National Natural Science Foundation of China (Grant No. 11962002 & 11902083 & 12072195), the Natural Science Foundation of Guangxi, China (Grant No. 2018GXNSFAA138205) and Innovation Project of Guangxi Graduate Education (YCBZ2021021).

Data availability The datasets/codes are available from the corresponding author on reasonable request.

Declarations

Conflict of interest The authors declare that they have no known competing financial interests or personal relationships

that could have appeared to influence the work reported in this paper.

References

1. Payne, H.J.: FREFLO: A macroscopic simulation model of freeway traffic. *Transp. Res. Rec.* **722**, 68–77 (1979)
2. Nagatani, T.: The physics of traffic jams. *Rep. Prog. Phys.* **65**, 1331–1386 (2002)
3. Zhang, H.M.: A theory of non-equilibrium traffic flow. *Transp. Res. Part B* **32**, 485–498 (1998)
4. Nagel, K., Schreckenberg, M.: A cellular automaton model for freeway traffic. *J. Phys.* **I(2)**, 2221–2229 (1992)
5. Mcdowell, M.: Kinetic theory of vehicular traffic. *J. Oper. Res. Soc.* **23(4)**, 599–600 (2017)
6. Pipes, L.A.: An operational analysis of traffic dynamics. *J. Appl. Phys.* **24**, 274–281 (1953)
7. Newell, G.F.: Nonlinear effects in the dynamics of car following. *Oper. Res.* **9**, 209–229 (1961)
8. Bando, M., Hasebe, K., Nakayama, A., et al.: Dynamical model of traffic congestion and numerical simulation. *Phys. Rev. E* **51**, 1035 (1995)
9. Lighthill, M.J., St. R., Whitham, G.B.: On kinematic waves I. Flood movement in long rivers. *Math. Phys. Sci.* **229**, 281–316 (1955)
10. Richards, P.I.: Shock waves on the highway. *Oper. Res.* **4**, 42–51 (1956)
11. Payne, H.J.: Models of freeway traffic and control. *Math. Models Public Syst. Simul. Council.* **1**, 51–61 (1971)
12. Papageorgiou, M.: A hierarchical control system for freeway traffic. *Transp. Res. Part B Methodol.* **17(3)**, 251–261 (1983)
13. Kühne, R.D.: Macroscopic freeway model for dense traffic: stop-start waves and incident detection. *Int. Symp. Transp. Traffic Theory* **9**, 21–42 (1984)
14. Kerner, B.S., Konhäuser, P.: Structure and parameters of clusters in traffic flow. *Phys. Rev. E* **50(1)**, 54–83 (1994)
15. Lee, H.Y., Lee, H.W., Kim, D.: Dynamic states of a continuum traffic equation with on-ramp. *Phys. Rev. E* **59(5)**, 5101–5111 (1999)
16. Daganzo, C.F.: Requiem for second-order fluid approximations of traffic flow. *Transp. Res. Part B: Methodol.* **29(4)**, 277–286 (1995)
17. Kaur, R., Sharma, S.: Analysis of driver's characteristics on a curved road in a lattice model. *Phys. A* **471**, 59–67 (2017)
18. Redhu, P., Gupta, A.K.: Effect of forward looking sites on a multi-phase lattice hydrodynamic model. *Phys. A* **445**, 150–160 (2016)
19. Sharma, S.: Lattice hydrodynamic modeling of two-lane traffic flow with timid and aggressive driving behavior. *Phys. A* **421**, 401–411 (2015)
20. Redhu, P., Gupta, A.K.: Delayed-feedback control in a lattice hydrodynamic model. *Commun. Nonlinear Sci. Numer. Simulat.* **27**, 263–270 (2015)
21. Redhu, P., Gupta, A.K.: Jamming transitions and the effect of interruption probability in a lattice traffic flow model with passing. *Phys. A* **421**, 249–260 (2015)
22. Gupta, A.K., Sharma, S., Redhu, P.: Effect of multi-phase optimal velocity function on jamming transition in a lattice

- hydrodynamic model with passing. *Nonlinear Dyn.* **80**, 1091–1108 (2015)
23. Gupta, A.K., Redhu, P.: Analyses of the driver's anticipation effect in a new lattice hydrodynamic traffic flow model with passing. *Nonlinear Dyn.* **76**(2), 1001–1011 (2014)
 24. Gupta, A.K., Redhu, P.: Analyses of driver's anticipation effect in sensing relative flux in a new lattice model for two-lane traffic system. *Phys. A* **392**, 5622–5632 (2013)
 25. Kuang, H., et al.: An extended car-following model accounting for the honk effect and numerical tests. *Nonlinear Dyn.* **87**, 149–157 (2017)
 26. Qiang, X.H., Huang, L.: Traffic flow modeling in fog with cellular automata model. *Modern Phys. Lett. B.* **35**(11), 2150180(1)–2150180(14) (2021)
 27. Xue, Y., Zhang, Y.C., et al.: An extended macroscopic model for traffic flow on curved road and its numerical simulation. *Nonlinear Dyn.* **95**(4), 3295–3307 (2019)
 28. Kerner, B.S., Rehborn, H.: Experimental properties of phase transitions in traffic flow. *Phys. Rev. Lett.* **79**, 4030–4033 (1997)
 29. Helbing, D., Treiber, M.: Gas-kinetic-based traffic model explaining observed hysteretic phase transition. *Phys. Rev. Lett.* **81**, 3042–3045 (1998)
 30. Lee, H.Y., Lee, H.W., Kim, D.: Traffic states of a model highway with on-ramp. *Phys. A* **281**, 78–86 (2008)
 31. Komada, K., Masukura, S., Nagatani, T.: Effect of gravitational force upon traffic flow with gradients. *Phys. A* **388**, 2880–2894 (2009)
 32. Zhu, W.X., Yu, R.L.: Nonlinear analysis of traffic flow on a gradient highway. *Phys. A* **391**, 954–965 (2012)
 33. Wu, C.X., Zhang, P., Wong, S.C., Choi, K.: Steady-state traffic flow on a ring road with up- and down-slopes. *Phys. A* **403**, 85–93 (2014)
 34. Gupta, A.K., Sharma, S., Redhu, P.: Analyses of lattice traffic flow model on a gradient highway. *Commun. Theor. Phys.* **62**(3), 393–404 (2014)
 35. Kaur, R., Sharma, S.: Modeling and simulation of driver's anticipation effect in a two lane system on curved road with slope. *Phys. A* **499**, 110–120 (2018)
 36. Li, X.L., Song, T., Kuang, H., Dai, S.Q., et al.: Phase transition on speed limit traffic with slope. *Chin. Phys. B* **17**(8), 3014–3020 (2008)
 37. Yu, R.L., Zhang, C.H.: Slope effect in traffic flow with a speed difference. *Appl. Mech. Mater.* **361–363**, 2297–2303 (2013)
 38. Chen, J.Z., Peng, Z.Y., et al.: An extended lattice model for two-lane traffic flow with consideration of the slope effect. *Mod. Phys. Lett. B* **29**(05), 1550017–1550022 (2015)
 39. Tan, J.H., Gong, L., Qin, X.Q.: An extended car-following model considering the low visibility in fog on a highway with slopes. *Int. J. Mod. Phys. C* **30**(11), 1950090–1950096 (2019)
 40. Zhou, J., Shi, Z.K., Cao, J.L.: An extended traffic flow model on a gradient highway with the consideration of the relative velocity. *Nonlinear Dyn.* **78**(3), 1765–1779 (2014)
 41. Zhang, X.D., Xu, J.L., Liang, Q.Q., et al.: Modeling impacts of speed reduction on traffic efficiency on expressway up slope sections. *Sustainability* **12**(2), 587 (2020)
 42. Choi, S., Suh, J., Yeo, H.: Microscopic analysis of climbing lane performance at freeway up slope section. *Transp. Res. Proc.* **21**, 98–109 (2017)
 43. He, H.D., Lu, W.Z., Xue, Y.: Dynamic characteristics and simulation of traffic flow with slope. *Chin. Phys. B* **18**(7), 2703–2708 (2009)
 44. Wang, Q.Y., Cheng, R.J., Ge, H.X.: A new lattice hydrodynamic model accounting for the traffic interruption probability on a gradient highway. *Phys. Lett. A* **16**, 1879–1887 (2019)
 45. Kuang, H., et al.: An extended car-following model incorporating the effects of driver's memory and mean expected velocity field in ITS environment. *Int. J. Mod. Phys. C* **32**, 2150095 (2021)
 46. Kuang, H., et al.: An extended car-following model considering multi-anticipative average velocity effect under V2V environment. *Phys. A* **527**, 121268 (2019)
 47. Kuang, H., et al.: An extended car-following model accounting for the average headway effect in intelligent transportation system. *Phys. A* **471**, 778–787 (2017)
 48. Berg, P., Mason, A., Woods, A.: Continuum approach to car-following models. *Phys. Rev. E* **61**, 1056–1066 (2000)
 49. Helbing, D.: Derivation of non-local macroscopic traffic equations and consistent traffic pressures from microscopic car-following models. *Eur. Phys. J. B* **69**(4), 539–548 (2009)
 50. Gupta, A.K., Katiyar, V.K.: A new anisotropic continuum model for traffic flow. *Phys. A* **368**(2), 551–559 (2006)
 51. Gupta, A.K., Katiyar, V.K.: Analyses of shock waves and jams in traffic flow. *J. Phys. A: Math. Gen.* **38**, 4069–4083 (2005)
 52. Yi, J.G., Lin, H., Alvarez, L., Horowitz, R.: Stability of macroscopic traffic flow modeling through wavefront expansion. *Transp. Res. Part B* **37**, 661–679 (2003)
 53. Ou, Z.H., Dai, S.Q., Zhang, P., Dong, L.Y.: Nonlinear analysis in the Aw-Rascle anticipation model of traffic flow. *SIAM J. Appl. Math.* **67**(3), 605–618 (2007)
 54. Gupta, A.K., Sharma, S.: Nonlinear analysis of traffic jams in an anisotropic continuum model. *Chin. Phys. B* **11**, 160–168 (2010)
 55. Carrillo, F.A., Delgado, J., et al.: Traveling waves, catastrophes and bifurcations in a generic second order traffic flow model. *Int. J. Bifurcat. Chaos.* **23**, 1350191–1350207 (2013)
 56. Delgado, J., Saavedra, P.: Global bifurcation diagram for the Kerner-Konhauser traffic flow model. *Int. J. Bifurcat. Chaos.* **25**, 1550064–1550075 (2015)
 57. Gasser, I., Sirito, G., Werner, B.: Bifurcation analysis of a class of 'car following' traffic models. *Phys. D* **197**, 222–241 (2004)
 58. Orosz, G.: Hopf bifurcation calculations in delayed systems. *Period. Polytech.* **48**, 189–200 (2004)
 59. Orosz, G., Stepan, G.: Hopf bifurcation calculations in delayed systems with translational symmetry. *J. Nonlin. Sci.* **14**, 505–528 (2004)
 60. Orosz, G., Stepan, G.: Subcritical Hopf bifurcations in a car-following model with reaction-time delay. *Proc. R. Soc. A* **462**, 2643–2670 (2006)
 61. Ngoduy, D., Li, T.: Hopf bifurcation structure of a generic car-following model with multiple time delays. *Transp. A: Transp. Sci.* **17**, 878–896 (2020)
 62. Ai, W.H., Shi, Z.K., Liu, D.W.: Bifurcation analysis of a speed gradient continuum traffic flow model. *Phys. A* **437**, 418–429 (2015)

63. Miura, Y., Sugiyama, Y.: Coarse analysis of collective behaviors: Bifurcation analysis of the optimal velocity model for traffic jam formation. *Phys. Lett. A* **381**, 3983–3988 (2017)
64. Ren, W.L., Cheng, R.J., Ge, H.X.: Bifurcation analysis of a heterogeneous continuum traffic flow model. *Appl. Math. Model.* **94**, 369–387 (2021)
65. Kerner, B.S., Konhäuser, P.: Cluster effect in initially homogeneous traffic flow. *Phys. Rev. E* **48**(4), R2335–R2338 (1993)
66. Cao, J.F., Han, C.Z., Fang, Y.W.: *Nonlinear Systems Theory and Application*. Xi'an Jiao Tong University Press, Xi'an (2006)
67. Herrmann, M., Kerner, B.S.: Local cluster effect in difference traffic flow models. *Phys. A* **255**, 163–188 (1998)
68. Igarashi, Y., Itoh, K., Nakanishi, K., et al.: Bifurcation phenomena in optimal velocity model for traffic flows. *Phys. Rev. E* **64**, 047102 (2001)

Publisher's Note Springer Nature remains neutral with regard to jurisdictional claims in published maps and institutional affiliations.

Springer Nature or its licensor (e.g. a society or other partner) holds exclusive rights to this article under a publishing agreement with the author(s) or other rightsholder(s); author self-archiving of the accepted manuscript version of this article is solely governed by the terms of such publishing agreement and applicable law.